BIOMECHANICS

Feedback-tracking microrheology in living cells

Kenji Nishizawa,[1]* Marcel Bremerich,[1]* Heev Ayade,[1] Christoph F. Schmidt,[2]† Takayuki Ariga,[1] Daisuke Mizuno[1]‡

Living cells are composed of active materials, in which forces are generated by the energy derived from metabolism. Forces and structures self-organize to shape the cell and drive its dynamic functions. Understanding the out-of-equilibrium mechanics is challenging because constituent materials, the cytoskeleton and the cytosol, are extraordinarily heterogeneous, and their physical properties are strongly affected by the internally generated forces. We have analyzed dynamics inside two types of eukaryotic cells, fibroblasts and epithelial-like HeLa cells, with simultaneous active and passive microrheology using laser interferometry and optical trapping technology. We developed a method to track microscopic probes stably in cells in the presence of vigorous cytoplasmic fluctuations, by using smooth three-dimensional (3D) feedback of a piezo-actuated sample stage. To interpret the data, we present a theory that adapts the fluctuation-dissipation theorem (FDT) to out-of-equilibrium systems that are subjected to positional feedback, which introduces an additional nonequilibrium effect. We discuss the interplay between material properties and nonthermal force fluctuations in the living cells that we quantify through the violations of the FDT. In adherent fibroblasts, we observed a well-known polymer network viscoelastic response where the complex shear modulus scales as $G^* \propto (-i\omega)^{3/4}$. In the more 3D confluent epithelial cells, we found glassy mechanics with $G^* \propto (-i\omega)^{1/2}$ that we attribute to glassy dynamics in the cytosol. The glassy state in living cells shows characteristics that appear distinct from classical glasses and unique to nonequilibrium materials that are activated by molecular motors.

INTRODUCTION

The complex interior of a biological cell is an active system because it is maintained away from thermodynamic equilibrium by internal energy dissipation and, in particular, by a variety of force-generating machineries (*1*, *2*). Two primary components determine the mechanics of a cell: the cytoskeleton, a network of semiflexible protein polymers, and the cytoplasm, a concentrated solution of biological macromolecules and organelles. These components govern the dynamics of cell functions and have characteristics of soft condensed materials (*3*, *4*). For decades, semiflexible polymers and soft glassy materials have been of central interest in materials science because of their complex mechanical properties (*5*–*10*). Both types of materials in cells alter their properties drastically in response to external perturbations; cytoskeletal networks typically stiffen under motor-generated mechanical stresses (*5*–*8*), whereas the glassy cytoplasm can be fluidized under mechanical load (*9*, *10*). In cells, metabolic activity generates chemical nonequilibrium, which powers mechanoenzymes (motor proteins). The functions of these mechanoenzymes are, in turn, influenced by their mechanical interactions with the surrounding materials (*11*, *12*). The dynamics of cellular constituents under these conditions obviously do not display equilibrium statistics. When investigating the mechanics of the interior of a living cell, it is therefore essential to clearly quantify the nonequilibrium activity.

Mechanical properties of macroscopic materials are typically measured by rheometers that apply a stress and measure the strain response or vice versa. A corresponding approach inside a cell is challenging because dimensions of cells are typically on the order of tens of micrometers. The method of choice in this case is microrheology (MR), in which micrometer-sized tracer beads are tracked and manipulated to probe the viscoelastic properties of their surroundings (*13*). Standard options of implementing MR include the passive tracking of bead fluctuations [passive MR (PMR)] (*14*–*17*) and active manipulation of the beads by known forces [active MR (AMR)] (*18*–*20*). The standard procedure used to calculate a material's viscoelasticity based on measured bead fluctuations (PMR) relies on the fluctuation-dissipation theorem (FDT) (*16*, *21*), which is only valid in thermodynamic equilibrium. However, mechanoenzymes in cells can create nonthermal fluctuations greatly in excess of thermal fluctuations (*1*, *2*, *22*). In such a situation, AMR can still be used to measure the mechanical response properties of the nonequilibrium system directly. Knowing the mechanical properties of the system then makes it possible to estimate the amplitude of the purely thermal fluctuations (*18*, *21*). Therefore, the combination of AMR and PMR allows one to separately quantify thermal and nonthermal fluctuations. The extent to which the FDT is violated is a novel metric that indicates how far the system is from thermodynamic equilibrium, owing to the dissipation of the internally transduced or externally injected mechanical energy (*22*–*24*). PMR in living cells has been performed, for instance, by recording videos of embedded probe particles (*25*, *26*). Although technically simple, video MR is lacking in both spatial and temporal resolution (*27*), and one cannot perform AMR. AMR in cells has rarely been conducted (*28*) because the strong motor-driven fluctuations make it difficult to exert a well-controlled force on the beads for a time that is sufficiently long to obtain a complete spectrum of response.

In previous in vitro (noncell) studies, simultaneous AMR and PMR were performed using optical trapping and laser interferometry technology (*2*, *18*, *24*). Two laser beams were focused on the probe particle: One was used to apply a sinusoidal force (optical trapping), and the other was used to detect the bead's position precisely relative to the laser focus (laser interferometry). There are several problems with applying this technology in living cells. In laser interferometry, the probe position is detected relative to the symmetry axis of the probe laser. The detection range is limited: The distance between the probe and the laser focus

[1]Department of Physics, Graduate School of Sciences, Kyushu University, 744 Motooka, Nishi-ku, Fukuoka 819-0395, Japan. [2]Third Institute of Physics, Faculty of Physics, University of Göttingen, Friedrich-Hund-Platz 1, 37077 Göttingen, Germany.
*These authors contributed equally to this work.
†Present address: Department of Physics, Duke University, Durham, NC 27708, USA.
‡Corresponding author. Email: mizuno@phys.kyushu-u.ac.jp

must remain sufficiently smaller than the radius of either the beam waist (~0.2 μm) or the probe particle (*29*). In metabolically active cells, a weakly trapped probe typically rapidly moves out of this range during observations. A strong optical trap could possibly maintain the probe in the trap, but large stresses would build up locally as a result of internal activities. It would then be impossible to determine the linear response mechanics of cells because cellular materials (cytoskeleton and cytoplasm) exhibit strongly nonlinear viscoelasticities (*5*, *7*, *30*). Increasing the radius of the beam waist extends the detection range (*29*) but reduces the laser diffraction efficiency and, therefore, the signal-to-noise ratio.

Here, we introduce a new method to solve this problem. We implemented three-dimensional (3D) feedback to smoothly reposition the piezo-actuated sample stage and the stage holding the objective lens to maintain the probe bead in the detection range. The total bead motion, which is the core observable for both AMR and PMR, can be obtained by summing the low-frequency stage movement and the high-frequency motion of the probe relative to the laser focus as determined by interferometry. Feedback-implemented MR successfully solved not only the problem of stably tracking probe beads in vigorously fluctuating environments but also another problem with conventional optical trapping MR, namely, that the low-frequency response (and fluctuations) of the probe are suppressed by the optical trapping potential (*18*, *31*), which makes it practically impossible to measure slow dynamics. This problem disappears in feedback-implemented MR. Because the feedback-controlled stage follows the slow motion of probe beads and always retains the beads in the laser focus, the bead motions at low frequencies are not affected by the optical trapping force. At higher frequencies, though, the optical trap exerts a time-varying force on the probe particle. In other words, the system is already driven out of equilibrium by the optical trapping force. Via the feedback mechanism, this driving force is correlated with the thermal forces. We provide a theoretical procedure that can be used to apply the FDT to correct for these artificial nonequilibrium effects due to feedback.

After validating the procedure by performing control experiments in equilibrium materials [polyacrylamide (PAAm) gels and entangled actin solutions], we applied feedback-enhanced AMR and PMR in cultured eukaryotic cells. At low frequencies, we observed a significant violation of the FDT. The nonthermal fluctuations were several orders of magnitude larger than the thermal fluctuations. These fluctuations reflect more or less correlated activity of motors at intermediate frequencies (*24*). Fluctuations typically become random at longer time scales such that the mean squared displacement scales linearly with time (*32*, *33*). Because the dominating driving forces for these random fluctuations are also nonthermal, as demonstrated by the breaking of the FDT, this motion is what has been referred to as "active diffusion" or "active stirring" (*22*, *32*, *34*). On the other hand, the high-frequency response in cells satisfies the FDT and exhibits a power-law behavior consistent with that predicted for semiflexible polymer gels in equilibrium (*7*, *18*) and colloidal glasses (*35*, *36*). Through mechanical experiments with isolated adherent fibroblast cells (which were flattened and, in the flat part of the cell, abundant in actin cytoskeleton), we found widely distributed elastic properties of such cells, as expected, which displayed the well-known viscoelastic behavior $G^* \propto (-i\omega)^{3/4}$ at high frequencies. In further experiments, we found that confluent sheets of epithelium-like HeLa cells showed highly reproducible viscoelasticity and a power-law behavior $G^* \propto (-i\omega)^{1/2}$ that is distinct from that exhibited by semiflexible polymers but is typically observed for soft glassy materials (*35*, *36*). We observed that the high-frequency shear modulus increased exponentially with cytosol concentration. To explain these observations, we suggest that one can model the HeLa cell epithelium as an actively stirred glass where the heterogeneous dynamics that typically appear in inactive glasses can continuously relax.

RESULTS

Theoretical foundation of feedback MR

Conventional AMR without feedback is explained in detail in note S1 (*18*) to provide the background for MR under feedback control. The experimental setup for feedback MR is shown in Fig. 1A, and its technical details are given in Materials and Methods. When the position of the sample stage is controlled by feedback, the total displacement u of the probe in the sample is given by $u = u_{QPD} + u_{stage}$, where u_{QPD} is the distance between the probe particle and the focus of the probe laser and u_{stage} is the displacement of the piezo stage, as shown in Fig. 1B. The optical trapping force applied to the probe particle by both the drive and probe lasers is given by $k_d L \exp(-i\omega t) - (k_d + k_p)u_{QPD}$, where L is the amplitude of the drive laser oscillation and k_d and k_p refer to the trap stiffnesses of the drive and probe lasers, respectively. The Langevin equation for the probe particle under feedback control is

$$k_p u_{QPD}(t) + \int_{-\infty}^{t} \gamma(t-t')\dot{u}(t')dt' = k_d(Le^{-i\omega t} - u_{QPD}(t)) + \zeta(t) + f(t) \quad (1)$$

where $\dot{u}(t)$ denotes the velocity of the probe in the coordinate system of the sample medium that is stationary with respect to the feedback-controlled piezo stage but moves in the lab frame. $\gamma(t)$ is the friction

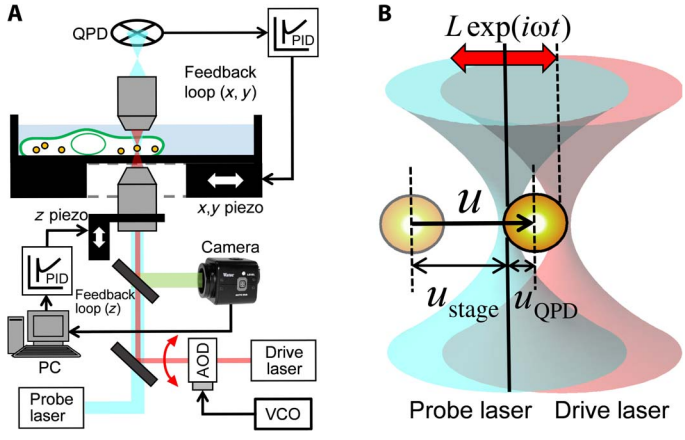

Fig. 1. Experimental setup for feedback MR. (**A**) Optical trap–based AMR setup with 3D feedback controls. A probe particle in a cell is trapped and oscillated by the drive laser (pink). QPD signals from the probe laser (cyan) are fed into PID controllers, which regulate piezo stage motion in *x* and *y* directions such that the trapped probe particle is maintained near the optical trap center. The bright-field image of the probe is simultaneously projected onto a charge-coupled device (CCD) camera [green thick line; light-emitting diode (LED) light source is omitted]. The image is analyzed on a personal computer (PC) to adjust the *z* position of the objective lens through a *z* direction piezo scanner. (**B**) Schematics for bead displacements and laser positions. Positions of fixed probe laser (830 nm, cyan) and acousto-optic deflector (AOD)–steered drive laser (1064 nm, pink) are shown by solid and dashed vertical lines, respectively. The drive laser is drawn displaced to the right of the probe laser. The pale particle indicates the probe starting position.

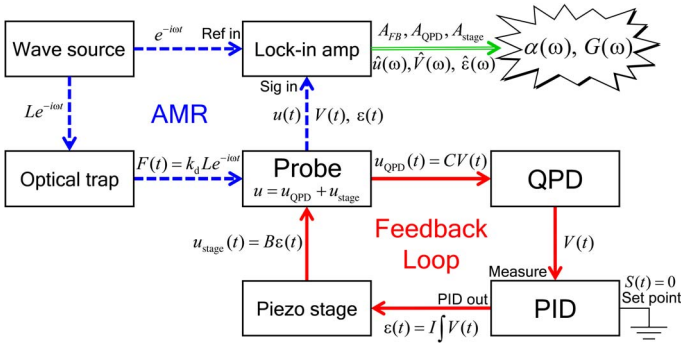

Fig. 2. Diagram of signal flow in AMR under feedback control. For AMR, feedback control of the piezo stage (red solid lines) is performed under sinusoidal force application to the probe particle with the drive laser (blue dashed lines). In PMR, the feedback loop is run without force application. $V(t)$ and/or $\varepsilon(t)$ is measured with a lock-in amplifier (AMR) or directly digitized and recorded by a PC (PMR).

function, and $\zeta(t)$ and $f(t)$ are the thermal and nonthermal forces, respectively. The ensemble average of Eq. 1 yields the frequency-dependent response, which is written as

$$\begin{aligned}\left\langle \hat{u}(\omega)\right\rangle^{\mathrm{FB}} &= \left\langle \hat{u}_{\mathrm{QPD}}(\omega)\right\rangle + \left\langle \hat{u}_{\mathrm{stage}}(\omega)\right\rangle \\ &= \alpha(\omega)\left\{\hat{F}(\omega) - (k_{\mathrm{d}}+k_{\mathrm{p}})\left\langle \hat{u}_{\mathrm{QPD}}(\omega)\right\rangle\right\} \end{aligned} \quad (2)$$

where $\alpha(\omega) = \alpha'(\omega) + i\alpha''(\omega) = 1/\left[-i\omega\tilde{\gamma}(\omega)\right]$ is the probe's response function without an optical trap. In Eq. 2, we have introduced an apparent driving force, $F(t) = k_{\mathrm{d}}Le^{-i\omega t} \equiv \hat{F}(\omega)e^{-i\omega t}$. Here and hereafter, the superscript "FB" indicates the total displacement when the position of the piezo stage is feedback-controlled; "~" and "^" denote the Fourier-transformed function and the amplitude of the sinusoidal signal, respectively; and angled brackets denote the statistical or time average.

For MR under feedback control, the output voltage $V(t) = u_{\mathrm{QPD}}/C$ of the quadrant photodiode (QPD) that detects the probe laser deflection is fed to the "Measure" input of an analog proportional-integral-derivative (PID) controller (Fig. 2). Here, $V(t)$ is the output voltage of the QPD, and C is the calibration factor for the displacement response of the QPD. The target value of $V(t)$ is the set point $s(t)$. On the basis of the error signal $V(t) - s(t)$, the PID controller generates a control signal $\varepsilon(t) = P(V-s) + I\int(V-s)dt + D\frac{d}{dt}(V-s)$, where P, I, and D are the respective weight factors for the three modes of feedback. Here, these feedback parameters were set so that only the second (integral) term is used to control the piezo stage ($P = D = 0$, $I \neq 0$). The set point $s(t)$ was set to 0, leading to the simple formula $\varepsilon(t) = I\int V dt$. Integrating the signal implies low-pass filtering and guarantees that the piezo stage can be controlled stably below its resonance frequency. We can then assume that u_{stage} responds to $\varepsilon(t)$ with a proportionality constant $B \equiv u_{\mathrm{stage}}(t)/\varepsilon(t)$. Thus

$$u_{\mathrm{stage}}(t) = B\varepsilon(t) = \frac{BI}{C}\int u_{\mathrm{QPD}}dt = \frac{1}{\tau}\int u_{\mathrm{QPD}}dt \quad (3)$$

where $\tau \equiv C/BI$ is the overall response time of our feedback-tracking system. Fourier-transforming $u = u_{\mathrm{QPD}} + u_{\mathrm{stage}}$ and Eq. 3 yields

$$\tilde{u} = \tilde{u}_{\mathrm{QPD}} + \tilde{u}_{\mathrm{stage}} = (1 - i\omega\tau)\tilde{u}_{\mathrm{stage}} = \left(1 - \frac{1}{i\omega\tau}\right)\tilde{u}_{\mathrm{QPD}} \quad (4)$$

The same relation holds for the sinusoidal responses, $\hat{u}(\omega)$, $\hat{u}_{\mathrm{QPD}}(\omega)$, and $\hat{u}_{\mathrm{stage}}(\omega)$, by changing ~ to ^. The stage displacement $u_{\mathrm{stage}}(t) = B\varepsilon(t)$ in response to the probe motion $u(t)$ is low-pass–filtered as $\tilde{u}_{\mathrm{stage}}(\omega)/\tilde{u}(\omega) = 1/(1 - i\omega\tau)$. The response time τ of the measurement system must be significantly longer than the response time of the piezo-actuated stage, which is approximately ~1 ms, as seen in Fig. 3B. The upper limit for useful low-pass filtering is set by the dynamics of the system and the detection range of the laser focus. The probe bead should not move more than about halfway through the detection range during the filter time. Therefore, τ was set typically between tens and hundreds of milliseconds (see fig. S1C).

We define the total response of the probe movement to the oscillatory force applied by the drive laser under feedback control as $A_{\mathrm{FB}} \equiv \langle\hat{u}(\omega)\rangle^{\mathrm{FB}}/\hat{F}(\omega)$. Using this definition and substituting Eq. 4 into Eq. 2, the following relationship between $A_{\mathrm{FB}}(\omega)$ and $\alpha(\omega)$ is obtained

$$A_{\mathrm{FB}}(\omega) = \frac{\langle\hat{u}(\omega)\rangle^{\mathrm{FB}}}{\hat{F}(\omega)} = \frac{\alpha(\omega)}{1 + \beta\alpha(\omega)} \quad (5)$$

where $\beta \equiv k_{\mathrm{t}}/(1 - 1/i\omega\tau)$ is the parameter describing the correction under feedback and k_{t} is the sum of the trap stiffnesses, $k_{\mathrm{t}} \equiv k_{\mathrm{d}} + k_{\mathrm{p}}$. The intrinsic response function $\alpha(\omega)$ can then be obtained from $A_{\mathrm{FB}}(\omega)$. From $\alpha(\omega)$, the complex shear modulus $G(\omega) = G'(\omega) + iG''(\omega)$ of the surrounding medium is obtained via the generalized Stokes relation (*13*, *37*)

$$G(\omega) = \frac{1}{6\pi a\alpha(\omega)} \quad (6)$$

where a is the radius of the probe particle.

Feedback AMR in thermal equilibrium

MR experiments with feedback were first tested in aqueous polymer networks in thermodynamic equilibrium, using tightly cross-linked PAAm gels and polystyrene beads with $2a = 2\,\mu$m diameter as probes. As illustrated in the signal diagram in Fig. 2, the electric signals $V(t) \propto u_{\mathrm{QPD}}$ and $\varepsilon(t) \propto u_{\mathrm{stage}}$ could be measured directly. Therefore, we define corresponding responses $A_{\mathrm{QPD}}(\omega) \equiv \left\langle\hat{u}_{\mathrm{QPD}}(\omega)\right\rangle/\hat{F}(\omega)$ and $A_{\mathrm{stage}}(\omega) \equiv \left\langle\hat{u}_{\mathrm{stage}}(\omega)\right\rangle/\hat{F}(\omega)$, as shown in Eqs. 10 and 12, respectively, in Materials and Methods. Figure 3A and fig. S2 depict the values of A_{QPD} (closed circles) and A_{stage} (open squares) that were measured using feedback AMR in PAAm. The spring constant for the effective potential that the probe particle experienced from the surrounding matrix was calculated from the shear modulus as $6\pi|G|a$ ($\geq 50 \times 10^{-6}$ N/m), which is considerably larger than the optical trap stiffness $k_{\mathrm{t}} = k_{\mathrm{p}} + k_{\mathrm{d}} = 6.8 \times 10^{-6}$ N/m. In this case, because the effect of k_{t} on the motion of the probe was negligible, α showed little difference from $A_{\mathrm{FB}} = A_{\mathrm{QPD}} + A_{\mathrm{stage}}$. In Fig. 3A, we present the values of α estimated from A_{QPD} and A_{stage} using Eqs. 11 and 13, as given in Materials and Methods. The rapid displacement of the probe is predominantly given by u_{QPD} ($u \sim u_{\mathrm{QPD}} \gg u_{\mathrm{stage}}$), and therefore, $\alpha \sim A_{\mathrm{QPD}}$ at high frequencies. On the other hand, the slow displacement

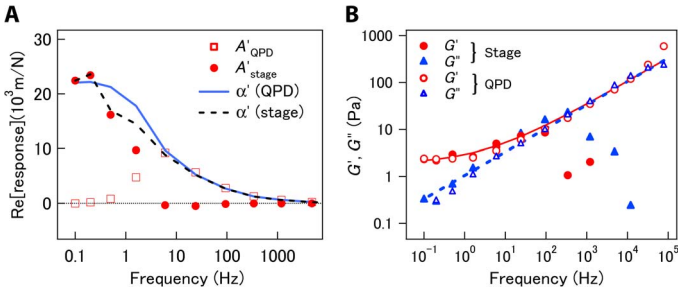

Fig. 3. Feedback AMR in equilibrium sample. (**A**) Real parts of response functions of probes embedded in a cross-linked PAAm gel, measured under feedback control. Open squares and filled circles indicate responses measured with QPD and stage, respectively. Solid and dashed curves show the estimated material response, α′, of the gel, as estimated from A'_{QPD} and A'_{stage}, respectively. (**B**) Complex shear modulus measured with AMR under feedback control (symbols) and fit of $G(\omega) = 1.9 + 0.59(-i\omega)^{1/2}$ (solid and dashed curves). Circles and triangles are real and imaginary parts of the modulus, respectively. Filled and open symbols correspond to moduli obtained using stage response and QPD response, respectively.

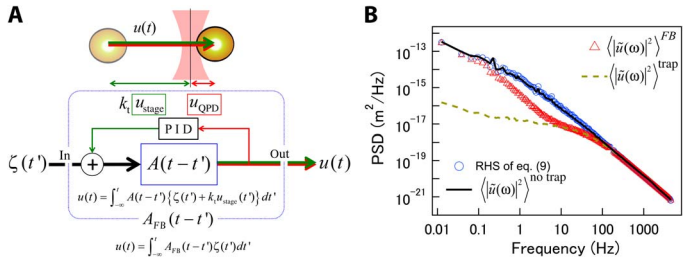

Fig. 4. Feedback PMR and conventional PMR. (**A**) Diagram of signal flow in PMR under feedback control. A_{FB} is the apparent response function in the time domain that relates (thermal) fluctuating force ζ(t′) and total probe displacement $u(t)$ under feedback. u_{QPD} and u_{stage} are correlated via the PID controller. A is the response function of the optically trapped probe in the absence of feedback. $k_t u_{stage}$ represents the reduction of the optical trapping force due to feedback. (**B**) Power spectral densities (PSDs) of displacement fluctuations of the probe embedded in entangled actin solution (1 mg/ml) measured with PMR. Open triangles and the dashed curve show PSDs directly measured with and without feedback, respectively. Open circles and the solid curve show $\langle|\tilde{u}(\omega)|^2\rangle^{no\ trap}$ calculated from $\langle|\tilde{u}(\omega)|^2\rangle^{FB}$ using Eq. 9 and PSDs calculated from $\langle|\tilde{u}(\omega)|^2\rangle^{trap}$ using the conventional PMR method, respectively.

is mostly given by the feedback-controlled displacement of the piezo stage ($u \sim u_{stage} \gg u_{QPD}$), such that $\alpha \sim A_{stage}$ at low frequencies. The crossover frequency between these limiting behaviors that is shown in Fig. 3A is consistent with the estimated system response (note S2), $f_c = 1/(2\tau\pi) \sim 4$ Hz.

Figure 3B presents the viscoelastic shear modulus of the PAAm gel. G_{QPD} and G_{stage} were estimated from A_{QPD} and A_{stage} using Eqs. 6, 11, and 13. The inertial effect due to the mass of the probe particle and the matrix surrounding it, which becomes prominent at high frequencies (>10 kHz), was taken into account, following the procedure described elsewhere (*7*, *18*). Reliable values were not obtained for G_{stage} at frequencies higher than 100 Hz. Otherwise, the values of G_{QPD} and G_{stage} are mostly consistent. The solid and broken curves are the fits of a function that assumed a low-frequency elastic plateau in addition to a high-frequency power law $G(\omega) = g_0 + g_1(-i\omega)^{1/2}$, following the classical Rouse model for cross-linked networks composed of flexible polymers (*38*).

Feedback PMR and artificial breaking of FDT

Next, we discuss feedback PMR, that is, probe fluctuations under feedback control for a sample in thermodynamic equilibrium. To perform feedback PMR, we turned off either the drive laser ($k_d = 0$) or its spatial oscillation ($L = 0$). In both cases, the probe laser was used to detect displacements. The feedback now manipulated the stage position to cancel the thermal displacements of the probe. The Langevin equation for the probe movements is then

$$k_t u_{QPD}(t) + \int_{-\infty}^{t} \gamma(t - t')\dot{u}(t')dt' = \zeta(t) \qquad (7)$$

The Fourier transform of Eq. 7 and the relation between $\tilde{u}$ and $\tilde{u}_{QPD}$ via the PID feedback (Eq. 3) lead to a linear relation between u and the thermally fluctuating force ζ (Fig. 4A): $\tilde{u} = A_{FB}(\omega)\tilde{\zeta}$. Note that this relation is similar to the response to the externally applied force that is given in Eq. 5. Even if there are no nonthermal forces generated in the sample, that is, even if $f(t) = 0$, the probe particle is subjected to the nonthermally fluctuating optical-trapping force because of the stage feedback. Suppose that the response A_{FB} and corresponding fluctuations $\langle|\tilde{u}(\omega)|^2\rangle^{FB}$ are measured without knowing whether an active feedback loop is present. In this case, it is tempting to expect that the FDT of the first kind would hold as $\langle|\tilde{u}(\omega)|^2\rangle^{FB} = 2k_B T A''_{FB}(\omega)/\omega$ (*16*, *21*). To investigate this assumption, we performed MR under feedback to estimate $\langle|\tilde{u}(\omega)|^2\rangle^{FB}$ and A''_{FB} independently using a material at thermal equilibrium, namely, an entangled actin network prepared at a concentration of 1 mg/ml in an aqueous buffer. Probe particles were trapped with $k_t = k_p = 4.8 \times 10^{-6}$ N/m, and their fluctuations were recorded with and without feedback. While $\langle|\tilde{u}(\omega)|^2\rangle^{FB}$ was measured directly, $A''_{FB}(\omega)$ was obtained by substituting $\alpha(\omega)$, k_t, and τ in Eq. 5 with their independently measured values. The violation of the FDT was evidenced by the clear disagreement between $\omega\langle|\tilde{u}(\omega)|^2\rangle^{FB}$ and $2k_B T A''_{FB}(\omega)$ (see fig. S3).

This violation of the FDT breaking is reasonable because the system was artificially driven out of equilibrium as a result of the imposed feedback, as schematically shown in Fig. 4A. Expressing the FDT as $\langle|\tilde{u}(\omega)|^2\rangle^{FB} = 2k_B T A''_{FB}(\omega)/\omega$ is therefore not correct. Fluctuations under feedback control are described by rewriting the Fourier transform of Eq. 7 as

$$\tilde{u}(\omega) = \frac{\alpha}{1 + k_t\alpha}(\tilde{\zeta} + k_t\tilde{u}_{stage}) = A(\omega)(\tilde{\zeta} + k_t\tilde{u}_{stage}) \qquad (8)$$

Here, $A(\omega)$ is the response of the optically trapped probe in the absence of feedback, which can be expressed as $A(\omega) = \alpha(\omega)/[1 + k_t\alpha(\omega)]$ [see note S1 (*18*, *31*)]. Equation 8 indicates that $\tilde{u}(\omega)$ is driven by $\tilde{\zeta}$ and the optical trapping force due to the movement of the piezo stage $k_t\tilde{u}_{stage}$ (the green arrow in Fig. 4A). The actual optical force applied to the probe is $-k_t u_{QPD}$, although $-k_t u = -k_t(u_{QPD} + u_{stage})$ would have been applied to the probe (see notes S1 and S3) were it not for the feedback. Therefore, the difference, $k_t u_{stage}$, is the driving force due to the feedback. The obvious consequence of the feedback is that the optical trapping force $k_t u_{QPD}(t)$ is strongly correlated with ζ(t); $\langle|\tilde{u}(\omega)|^2\rangle^{FB}$ is therefore not equal to the sum of the second moments for thermal and nonthermal fluctuations. In our previous studies that have reported the FDT violations in nonequilibrium systems (*1*, *2*, *18*, *24*), these correlations between thermal and nonthermal forces were assumed to not exist. However, supposing linear response, the statistical properties

of ζ should not be affected by the application of the additional force, $k_t u_{stage}$. Thus, ζ can be described using the FDT of the second kind as $\langle|\tilde{\zeta}(\omega)|^2\rangle = 2k_BT\mathrm{Re}\left[-1/i\omega A(\omega)\right] = 2k_BT\mathrm{Re}\left[-1/i\omega\alpha(\omega)\right]$. The PSD of the total displacement under feedback is given by $\langle|\tilde{u}(\omega)|^2\rangle^{FB} = |A_{FB}(\omega)|^2\langle|\tilde{\zeta}(\omega)|^2\rangle = |1/(1+\beta\alpha)|^2 2k_BT\alpha''/\omega$. By independently measuring α, it is possible to calculate the PSD in the absence of the optical trap potential as

$$\langle|\tilde{u}(\omega)|^2\rangle^{\text{no trap}} = |1+\beta\alpha(\omega)|^2\langle|\tilde{u}(\omega)|^2\rangle^{FB} \quad (9)$$

Here and hereafter, the superscript "no trap" denotes fluctuations measured in the absence of the optical trap.

The PSDs in the presence and absence of the optical trap, $\langle|\tilde{u}(\omega)|^2\rangle^{trap}$ and $\langle|\tilde{u}(\omega)|^2\rangle^{\text{no trap}}$, were measured by conventional PMR and are shown as broken and solid curves, respectively, in Fig. 4B. In conventional optical trap–based PMR experiments, the probe fluctuations are suppressed by the optical trap below the frequency at which $|k_tA(\omega)| \sim 1$ is reached. In Fig. 4B, this crossover is observed at around 100 Hz, and $\langle|\tilde{u}(\omega)|^2\rangle^{\text{no trap}}$ and $\langle|\tilde{u}(\omega)|^2\rangle^{trap}$ are distinct at lower frequencies. In feedback PMR, the total fluctuations of the probe, $u(t)$ $[=u_{QPD}(t) + u_{stage}(t)]$, can be reconstructed, and the power spectrum $\langle|\tilde{u}(\omega)|^2\rangle^{FB}$ (red triangles in Fig. 4B) shows additional features. In this case, another crossover between $\langle|\tilde{u}(\omega)|^2\rangle^{FB}$ and $\langle|\tilde{u}(\omega)|^2\rangle^{trap}$ is observed at $f_c = 1/2\pi\tau \sim 10$ Hz. Below this frequency, $\langle|\tilde{u}(\omega)|^2\rangle^{FB}$ deviates from $\langle|\tilde{u}(\omega)|^2\rangle^{trap}$ and approaches $\langle|\tilde{u}(\omega)|^2\rangle^{\text{no trap}}$ because the slow motions of the probe, which the feedback follows, are less affected by the optical trap. By obtaining α by conventional PMR (note S3), we calculated the right-hand side of Eq. 9 (blue circles in Fig. 4B). Note that k_t and τ, which were necessary to evaluate β, were obtained by independent calibration (see Materials and Methods and note S2). The exact agreement between $\langle|\tilde{u}(\omega)|^2\rangle^{\text{no trap}}$ obtained using conventional and feedback PMR (the solid curve and circles in Fig. 4B) validates our analysis procedure.

Intracellular mechanics measured with feedback MR

After testing the proposed method in equilibrium systems, we performed MR experiments with feedback in living cells. Melamine particles with a high refractive index (and a diameter of $2a = 0.68$ μm) were first incorporated into NIH-3T3 fibroblast cells via phagocytosis. The total probe displacement $u(t) = u_{QPD}(t) + u_{stage}(t)$ is shown in Fig. 5A. The feedback maintains the probe in the detection range (~100 nm) for hours, which is sufficiently long to complete AMR experiments, whereas the total fluctuations become larger than the detection range in less than 30 s. The frequency dependence of $G(\omega)$, which was calculated via Eqs. 6 and 11, is shown in Fig. 5B. Because the refractive index profile of the cells is more or less inhomogeneous and distinct from the refractive index of the aqueous solvent, k_p and k_d were measured in situ for each particle in the cells, following the procedure described in note S4. Because the fluctuations and responses of probes ingested by phagocytosis into cells vary significantly, statistical averaging smears out characteristic features of each spectrum, such as relaxation times and power-law exponents. Therefore, a typical result that was fitted by the simple sum of two independent power laws, $G(\omega) \sim 140(i\omega)^{0.12} + (i\omega)^{0.74}$, is shown by the solid curves in Fig. 5B. However, note that the exponents and the prefactors vary from cell to cell and with

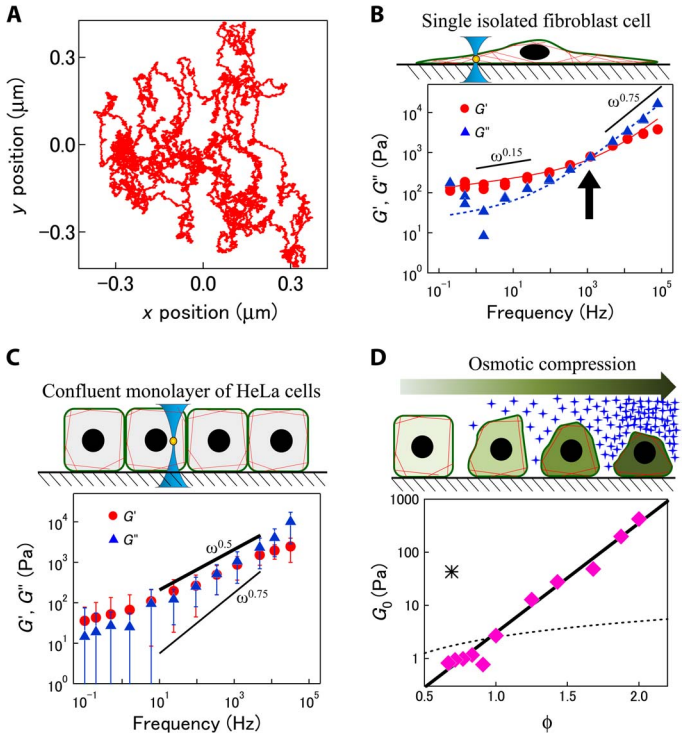

Fig. 5. Material properties of fibroblasts and HeLa cells measured with feedback MR. (**A**) 2D trajectory of a probe in a cell measured under feedback. The total period of observation was ~30 min. (**B**) Shear modulus measured in the peripheral region of an adherent fibroblast, which is rich in actin cytoskeleton. Solid and dashed curves are fits of an empirical model describing low-frequency relaxations and high-frequency power-law behavior of a semiflexible polymer network as $G(\omega) \sim 140(i\omega)^{0.12} + (i\omega)^{0.74}$. (**C**) Shear modulus measured in confluent HeLa cells ($n = 9$ cells cultured in different dishes). Bars indicate the unbiased estimate of the SD. Power-law form of viscoelasticities $G(\omega) \propto (-i\omega)^{0.5}$ indicates a glassy response of (actin network–poor) cytosol. (**D**) G_0 for osmotically compressed HeLa cells (pink diamonds) plotted against macromolecular concentration relative to isotonic condition ($\phi = 1$). Exponential dependence on macromolecule concentrations ϕ (solid line, exponential; dashed curve, linear dependence) is typical of strong glass formers rather than polymer networks. The asterisk marks G_0 for the cell extract taken from HeLa cells (0.21 g/ml).

the position of probe particles in the cells. In particular, noncoated probes phagocytosed into cells are likely surrounded by plasma membranes that can interact with rigid intracellular constituents. Depending on the intracellular structures to which a probe binds, responses will broadly vary. This opens an interesting option for future experiments where one could specifically target specific cell compartments, such as the nucleus, the endoplasmic reticulum, or the Golgi apparatus, by coating the beads with, for example, antibodies.

As a first step in the study of intracellular mechanics, we instead chose another approach: We coated the surfaces of the probe beads with polyethylene glycol (PEG) strands (*39*) and then bombarded cells with the probe beads using a gene gun (*40*). In aqueous environments, PEG coating generally passivates probe surfaces. The hydrophilic PEG creates repulsive interactions with both hydrophilic and hydrophobic biopolymers and prevents sticking to cytoskeletal elements and other proteins in cells (*41*). We prepared an epithelium-like sheet of confluent HeLa cells and used melamine particles (with a diameter of $2a = 1$ μm) incorporated at the center between the cell membrane and the nucleus

as probes. With this preparation, we found that the distribution of the mechanical properties measured was narrow, showing quantitatively similar behaviors among different HeLa cells (n = 9, Fig. 5C). Unlike isolated fibroblasts, G' and G'' in the confluent epithelium vary as a simple power law $G(\omega) = G_0(-i\omega)^{0.5}$ in a wide range of frequencies (Fig. 5C and fig. S4). The concentration dependence of G_0 helps to explain this unexpected power-law exponent in living epithelium as explained in detail in Discussion. Because high-frequency fluctuations in cells are purely thermal, as will be discussed below, we obtained the concentration dependence of the prefactor G_0 with feedback PMR. To vary intracellular concentration, we osmotically compressed (or dilated) the cells by adding sucrose (or water) to the culture medium. G_0 was found to be exponentially dependent on the concentration of macromolecules in HeLa cells (Fig. 5D). The same frequency dependence $G(\omega) = G_0(-i\omega)^{0.5}$ was also found in control experiments with HeLa cell extracts at a close to physiological concentration. The resulting G_0 for the cell extracts is shown by the asterisk in Fig. 5D.

Feedback PMR and FDT violation in living cells

We now compare feedback PMR and AMR results that were obtained simultaneously in NIH-3T3 cells. Figure 6A shows displacements u_{QPD} and u_{stage} in the x direction. We evaluated the PSDs of the probe displacement signals, such as $\langle|\tilde{u}(\omega)|^2\rangle^{FB}$, $\langle|\tilde{u}_{QPD}(\omega)|^2\rangle$, and $\langle|\tilde{u}_{stage}(\omega)|^2\rangle$ (Fig. 6B). We observed that $\langle|\tilde{u}(\omega)|^2\rangle^{FB}$ was obtained by simply summing $\langle|\tilde{u}_{QPD}(\omega)|^2\rangle$ and $\langle|\tilde{u}_{stage}(\omega)|^2\rangle$. This relationship stems from the fact that $\tilde{u}_{QPD}$ and $\tilde{u}_{stage}$ are correlated with a phase difference of $\pi/2$ because $\tilde{u}_{stage} = -\tilde{u}_{QPD}/i\omega\tau$, as shown in Eq. 3. The same relation was also observed in a sample in thermodynamic equilibrium (fig. S5). The response time of the feedback-tracking system in these experiments for NIH-3T3 cells, τ = 0.145 s, was measured independently, as illustrated in fig. S1A. This response time corresponds to a crossover between $\langle|\tilde{u}_{QPD}(\omega)|^2\rangle$ and $\langle|\tilde{u}_{stage}(\omega)|^2\rangle$ at $f_c \sim 1.1$ Hz. The same probe particle was also tracked without feedback, and the resulting $\langle|\tilde{u}(\omega)|^2\rangle^{trap}$ is shown in Fig. 6B. Without feedback, the bandwidth of $\langle|\tilde{u}(\omega)|^2\rangle^{trap}$ is limited at low frequencies because the particle could not be tracked for longer than several tens of seconds in any of the trials. In the measured frequency range, $\langle|\tilde{u}(\omega)|^2\rangle^{trap}$ and $\langle|\tilde{u}(\omega)|^2\rangle^{FB}$ are consistent.

The imaginary parts α'' of the response functions that were obtained with AMR and PMR using the expression $\omega\langle|\tilde{u}(\omega)|^2\rangle^{no\ trap}/2k_BT$ are shown in Fig. 7A. The agreement of these functions at frequencies higher than ~10 Hz indicates that the FDT is satisfied here, whereas the obvious discrepancy demonstrates the breaking of the FDT at lower frequencies (*1*, *2*, *18*, *24*). The PSD of the nonthermal fluctuations was obtained using Eq. 15, by subtracting the thermal fluctuations from the total fluctuations. The resulting function $\omega\langle|\tilde{u}(\omega)|^2\rangle^{nonthermal}/2k_BT$ is shown by the solid curve in Fig. 7A. Attempts to deduce nonthermal forces from $\langle|\tilde{u}(\omega)|^2\rangle^{nonthermal}$ have been reported earlier (*1*, *18*, *22*) and repeated recently (*28*, *42*, *43*). In these studies, the probe motion was described using the Langevin equation $\int_{-\infty}^{t}\gamma(t-t')\dot{u}(t')dt' = \zeta(t) + f(t)$. Assuming that $\zeta(t)$ and $f(t)$ are not correlated, taking the Fourier transform of the statistical average immediately gives $\langle|\tilde{u}(\omega)|^2\rangle^{nonthermal} = |\alpha(\omega)|^2\langle|\tilde{f}(\omega)|^2\rangle$.

In general viscoelastic materials, thermal fluctuations exhibit power-law scaling $\omega\langle|\tilde{u}(\omega)|^2\rangle^{nonthermal} \propto \omega^{\nu}$, where the exponent ν is limited to the range $-1 \le \nu \le 1$. The exponent for Brownian motion or simple diffusion is $\nu = -1$. This limitation does not necessarily hold for nonthermal fluctuations. The inset in Fig. 7A shows the power-law exponents of the nonthermal fluctuations $\omega\langle|\tilde{u}(\omega)|^2\rangle^{nonthermal}$ that were calculated at each frequency using $d\log\omega\langle|\tilde{u}(\omega)|^2\rangle^{nonthermal}/d\log\omega$. At frequencies 0.1 Hz < f < 10 Hz, exponents smaller than −1 were observed, exceeding the lower limit of ν for equilibrium systems. This is likely due to the directed transport of the probe as seen in the 2D probe trajectory (Fig. 5A). Transport direction memory becomes evident in the calculation of the autocorrelation function for the velocity direction $\vec{n}(t)$ (Fig. 7B). The nonzero autocorrelation confirms that the motion is directed, but the direction memory was lost at around 1 s for this sample. Directed transport, sometimes called "super-diffusion," is another indication of an out-of-equilibrium situation and typically results from motor protein activity in cells.

DISCUSSION

In cells, molecular motors such as myosins generate forces that induce nonthermal fluctuations that are tracked by our probe particles. Nonmuscle cytoplasmic myosins bind to actin and progressively build up stress in the network with correlation times on the order of seconds.

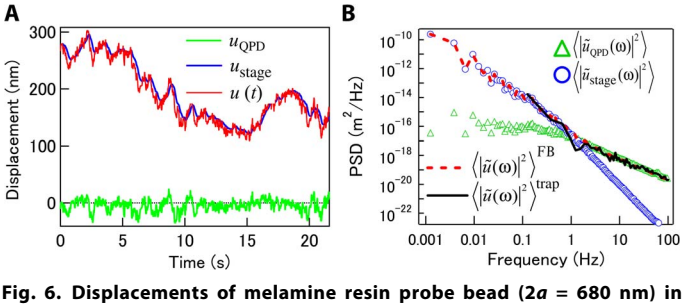

Fig. 6. Displacements of melamine resin probe bead (2*a* = 680 nm) in cultured fibroblast cell (NIH-3T3). (**A**) QPD and control signals for piezo stage as output by PID controller were recorded and calibrated to obtain displacements u_{QPD} (green) and u_{stage} (blue), respectively. Total displacement u(t) (red) was obtained by summing these quantities. (**B**) The displacement PSD measured using QPD with conventional PMR (black curve) agrees with that obtained under feedback by summing u_{QPD} and u_{stage}.

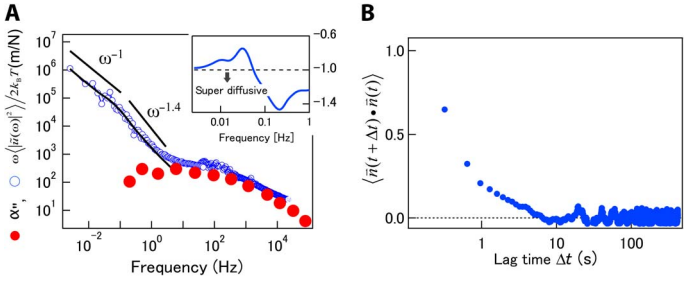

Fig. 7. FDT violation and out-of-equilibrium fluctuations in a fibroblast cell. (**A**) Imaginary part of the complex response function measured inside a fibroblast using feedback AMR, compared to the corresponding function $\omega\langle|\tilde{u}(\omega)|^2\rangle^{no\ trap}/2k_BT$ measured with PMR. Curves agree at high frequencies and clearly differ at frequencies less than 10 Hz. The solid curve shows purely nonthermal fluctuations calculated using Eq. 15. Solid lines show power laws for comparison. Inset: Local power-law exponent of nonthermal fluctuations calculated using $d\log\omega\langle|\tilde{u}(\omega)|^2\rangle^{nonthermal}/d\log\omega$. Crossover between different scaling regimes can be observed. (**B**) Autocorrelation function of velocity direction.

Myosins then stochastically unbind from the actin filaments and thereby instantaneously release stress stored in the elastic network (*2*, *6*, *44*). These motor-induced fluctuations have been studied in reconstituted actin/myosin gels where the abrupt stress release causes directed motion of probes (fig. S6A) (*2*, *44*). Considering the standard relation between step response and the frequency response of a material, the correlation time τ_1 of the directed motion can be estimated from the angular frequency ω_1 ($\sim 1/\tau_1$), where $G'(\omega_1) = G''(\omega_1)$ (see fig. S6B and the discussion thereof). The abrupt release of stress corresponds to a step in $f(t)$ in Eq. 1 and, therefore, on average $\left\langle |\tilde{f}(\omega)|^2 \right\rangle \propto \omega^{-2}$ in Eq. 15 if such events occur in an uncorrelated manner (*45*). The nonthermal fluctuations derived from measuring both $\left\langle |\tilde{u}(\omega)|^2 \right\rangle^{\mathrm{nonthermal}}$ and $\alpha(\omega)$ (*18*, *24*) were consistently explained by inserting this power-law dependency into Eq. 15: $\left\langle |\tilde{u}(\omega)|^2 \right\rangle^{\mathrm{nonthermal}} = |\alpha(\omega)|^2 \left\langle |\tilde{f}(\omega)|^2 \right\rangle$. The same discussion was speculated to hold for nonthermal fluctuations in living cells (*28*). A viscoelastic response function in the cell of the form $|\alpha(\omega)|^2 \propto 1/|G(\omega)|^2 \propto \omega^{-0.36}$ at frequencies less than 10 Hz (Fig. 5B) would lead to $\omega \left\langle |\tilde{u}(\omega)|^2 \right\rangle^{\mathrm{nonthermal}} \propto \omega |\alpha(\omega)|^2 \left\langle |\tilde{f}(\omega)|^2 \right\rangle \propto \omega^{-1.36}$, which was close to the observed relationship $\omega \left\langle |\tilde{u}(\omega)|^2 \right\rangle^{\mathrm{nonthermal}} \propto \omega^{-1.4}$. However, note that the actual correlation time of the directed motions observed in cells (>1 s) is much longer than the estimate $\tau_1 \leq 1$ ms based on the abrupt stress-release model (see the arrow in Fig. 5B for the estimate of ω_1). The assumption of uncorrelated motor activity is thus likely to neglect important aspects of intracellular activity. A more realistic interpretation of the directed fluctuations (super-diffusion) observed in cells is that the probes are driven by collective and correlated force generation. The collective action of force generators likely persistently stirs the cytoplasm on relatively long time scales, so that the memory of force is not lost immediately after a single motor detaches from the cytoskeleton. At longer time scales ($\omega/2\pi < 0.1$ Hz), the displacement PSDs show power-law behavior (Fig. 7A, inset) similar to that of simple diffusion in a viscous medium, $\omega \left\langle |\tilde{u}(\omega)|^2 \right\rangle^{\mathrm{no\ trap}} / 2k_B T = \alpha''(\omega) \propto \omega^{-1}$ (*22*, *31*, *33*). However, the slope of −1 here does not imply thermal diffusion because the probe is driven by nonthermal forces, as proven by the breaking of the FDT. Probes moving in cells lose their velocity memory on the same time scale (≥ 1 s). The slope of −1 is thus due to the Markovian nature of probe displacements driven by cells.

The high-frequency shear modulus of the fibroblast cell $\propto (-i\omega)^{0.74}$ observed in Fig. 5B is consistent with theoretical predictions $\propto (-i\omega)^{3/4}$ for networks of semiflexible polymers such as the cytoskeleton (*46*, *47*). Isolated fibroblast cells that are sparsely cultured on glass coverslips acquire flattened shapes, adhere well to the substrate, and grow F-actin–rich cross-linked cytoskeletal structures (*48*), which should resemble pure actin networks in their response characteristics. At low frequencies, mechanical response is predominantly elastic ($G' >> G''$) but shows slow relaxation with small power-law exponents around 0.2±0.1 (*3*, *4*, *49*). A similar behavior has been observed in various random networks of polymers (*7*, *18*) and has been explained by nonaffine relaxations (*7*) in glassy worm-like chains (*10*, *50*). These theoretical models have also successfully explained the mechanical responses of cells to forces that were applied from the outside (*1*, *3*, *4*, *49*). Our study reveals that the same general physics appears to apply to the viscoelastic response inside of cytoskeleton-rich living cells.

HeLa cells in confluent layers, in contrast to well-spread fibroblasts, are laterally confined and polarized. They are roughly as tall as they are wide, and the actin cytoskeleton is mostly confined to the membrane cortex from which our probe particles were sufficiently separated (*51*, *52*). The response measured in different HeLa cells showed a surprisingly narrow distribution, especially at high frequencies. We could clearly show that the power-law form of the shear modulus $G(\omega) \sim G_0(-i\omega)^{0.5}$ (Fig. 5C) was distinct from the two regimes $G(\omega) \propto (-i\omega)^{0.2 \pm 0.1}$ and $G(\omega) \propto (-i\omega)^{0.75}$ observed in surface-adherent fibroblasts (solid lines in Fig. 5B). The power-law dependence [$G(\omega) \propto G_0(-i\omega)^{0.5}$] is a well-known characteristic of glassy suspensions of colloids with nonsticky surfaces such as emulsions, foams, and swollen microgels (*35*, *36*). Thus, the mechanics of the interior of living confluent epithelial cells that is sparse in cytoskeletal network structure are likely better modeled as a soft glassy material (*3*, *10*). Note that a model for soft glassy materials was also used earlier to explain the results of low-frequency cell mechanics experiments (*3*). In that case, a $G(\omega) \propto (-i\omega)^{0.2 \pm 0.1}$ power law was found for the slow response of the actin cytoskeleton, caused by cross-link constraint release. Here, we report the expected three-fourths scaling $G(\omega) \propto (-i\omega)^{0.75}$ at higher frequencies when probing the actin cytoskeleton in flattened fibroblasts. This is a very different physical situation from the one we describe here for the inside of the epithelial cells where we see, in the same frequency range, a quite different response $G(\omega) \propto G_0(-i\omega)^{0.5}$ in the highly crowded glassy but not network-like cytoplasm.

A power-law dependence $G(\omega) \propto G_0(-i\omega)^{0.5}$ has also been observed in networks of flexible polymers for which the Rouse model applies (*2*, *38*, *46*). The concentration dependence of the shear modulus prefactor (G_0) provides a way to distinguish between a flexible polymer network and colloidal glass. For a Rouse network, G_0 is proportional to the polymer concentration (*38*, *46*). In contrast, close to the glass transition of glass-forming materials, viscoelastic moduli grow more rapidly than linear increase (*53*). To probe concentration dependence, we osmotically compressed or expanded cells that were initially in isotonic conditions and measured the shear modulus as a function of relative intracellular macromolecular concentration (Fig. 5D). The measured G_0 increased exponentially with the macromolecular concentration ϕ in HeLa cells, which is inconsistent with Rouse polymer networks (*38*, *46*). The more plausible explanation for this dependence is thus that the mechanics inside confluent HeLa cells are predominantly determined by the glassy cytosol that is tightly packed with biomolecular colloids and approaches a jamming transition (*54*).

It has been speculated that crowding in cells containing high concentrations of macromolecules (proteins, RNA, and organelles) affects cell mechanics (*55*, *56*). The exponential dependence of G_0 on the macromolecule concentration is reminiscent of that of strong glass formers made of soft colloids (*57*). It was shown that the viscoelasticity of extracted cytosol increases much more rapidly than the cytosol of the living cell, namely, with a super-exponential dependence on ϕ. In addition, the absolute value of G_0 of extracted cytosol, which lacks nonequilibrium stress fluctuations, is far larger than that we see in living cells (see the asterisk in Fig. 5D). This comparison leads us to speculate that the out-of-equilibrium activity in the cell might be responsible for both the weaker viscoelastic response and the exponential (as opposed to super-exponential) concentration dependence. Super-exponential dependency is a typical consequence of jamming in tightly packed rigid colloids. Frustration of local arrangements leads to inhomogeneous distributions of residual forces and stresses in the sample, which can only relax through rare cooperative rearrangements. Therefore, the exponential increase of viscosity might be explained by active stirring in cells (*2*) that can release and homogenize the locally frozen stresses. Active stirring should also make the living HeLa cells respond more homogeneously than expected, explaining the surprisingly narrow distribution of measured viscoelasticities (fig. S4).

The mechanical response of many biomaterials is not well understood, even in thermodynamic equilibrium. In cells, mechanical responses are often further modulated by cell activity. Motor-generated forces, for instance, stiffen cytoskeletal networks in vitro and in vivo until the network structure is broken by excessive stress (*2*, *6*, *18*, *42*). Cytoskeletal networks in cells are also thought to undergo sol-gel transitions when self-organized contractile stresses drive cytoplasmic flows (*58*, *59*). Our feedback MR experiments in epithelial-like HeLa cells revealed that the living cytoplasm exhibits glass-like behavior. This provides a critical role for active stress generation in the cell. The cytoplasm can be fluidized by activity just as colloidal glasses and granular materials are under mechanical loads or external perturbations (*54*, *60*). It will be crucial to understand in detail how the nonthermal fluctuations in cells determine the mechanical properties of living cells (*22*, *24*). A precise quantitative analysis of the out-of-equilibrium mechanics in cells, as can be performed with the approach presented here, will be essential to further investigate the fascinating interplay between cellular mechanics and nonequilibrium force generation.

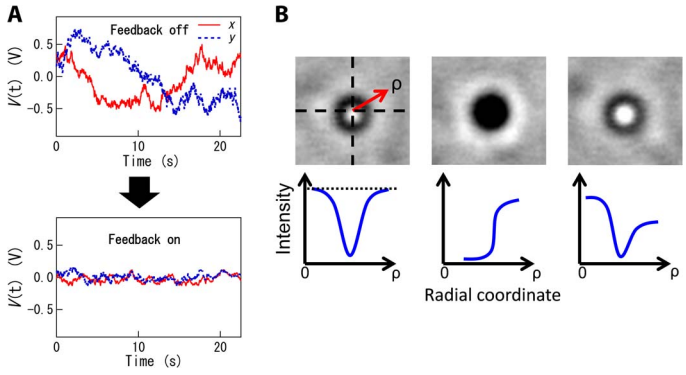

Fig. 8. 3D feedback. (**A**) Typical voltage time series recorded by the QPD with or without feedback, obtained with a probe embedded in a fibroblast cell. Strong fluctuations of the QPD signal (top) are suppressed when feedback is active (bottom). (**B**) The radial distribution of probe image brightness is used for feedback control of the *z* position of the objective lens. Top images show probe patterns, and bottom images schematically show typical intensity profiles in radial coordinates. *z* position is controlled such that the brightness at the fringe and in the center of the pattern remains equal (dotted line).

MATERIALS AND METHODS

Conventional AMR and PMR

The details of the experimental setup for conventional MR using optical traps and laser interferometry without feedback control are given in detail elsewhere (*18*) (see notes S1 and S3). Briefly, the setup consists of two optical traps generated by lasers of two different wavelengths (Fig. 1, A and B). In the AMR study, one of the lasers (λ = 1064 nm, Nd:YVO4, Compass, Coherent) was operated as the drive laser and was deflected by an AOD (model DTSX-400-1064, AA Opto-Electronic SA), which was sinusoidally driven by a voltage-controlled oscillator (model AA. DRF. 40, Opto-Electronic SA). The other laser (λ = 830 nm, IQ1C140, Power Technology) was used as the probe laser, remained stationary during operation, and was used to detect the position of the same probe particle by back-focal-plane laser interferometry (*14*, *15*, *28*). Angular intensity shifts of the probe laser light due to the displacement of the probe particle were detected with a QPD (SPOT9D, OSI Optoelectronics AS). The output signal from the QPD, which was synchronous with the oscillations, was measured using a lock-in amplifier (Model 7225, Signal Recovery). For the PMR experiments, the oscillation of the drive laser was turned off, and the thermal and/or nonthermal spontaneous motions of the probe particles were detected by laser interferometry. The output signal from the QPD was digitized at 100 kHz with an A/D board (AD24 DSA board PCI-4462, National Instruments) and recorded on a PC.

3D feedback

Slow movements of probe particles were compensated for in three dimensions by feedback loops controlling the position of the sample stage (in the *x* and *y* directions) and the objective lens (in the *z* direction). As shown in Fig. 1A, the in-plane (*x* and *y*) displacements of the probe particle were measured using laser interferometry, as described above. The voltage signals for both the *x* and *y* displacements that were output from the QPD were fed into two analog PID controllers (SIM960, 100 kHz, Stanford Research Systems Inc.), with the "set point" inputs grounded using BNC grounding caps. The controller outputs were connected to the 2D piezo stage [SFS-120XY(WA), SIGMAKOKI] on which the sample chamber was mounted. For slow probe particle movements, this feedback loop repositioned the piezo stage such that the bead always remained near the center of the laser focus (Fig. 8A). We denote the piezo stage displacement as u_{stage}. The voltages output by the QPD and PID controllers [$V(t)$ and $\varepsilon(t)$, respectively] were recorded on a PC with a 24-bit A/D board (NI-PCI-4462, National Instruments) and were separately calibrated to u_{QPD} and u_{stage}, respectively (as described in the next section). The total displacement of the probe bead in the sample chamber was then obtained as $u \equiv u_{QPD} + u_{stage}$ (Fig. 1B).

Slow out-of-plane (*z* direction) movements of a probe particle, which would affect the stiffness of the optical trap and the sensitivity of the QPD output to the in-plane (*x* and *y*) displacements, were compensated for by feedback control of the *z* position of the objective lens (Fig. 1A). Out-of-plane movements of a probe particle were detected by analyzing the patterns in the bead images that were projected onto a CCD camera (WAT-902B, Watec). The microscope images of the beads were collected with an image-capture board (IMAQ PCI-1408, National Instruments) and analyzed in real time by custom-written software (LabVIEW 8.6, National Instruments). First, the center-of-mass position of each probe particle was obtained on the basis of the pattern in the corresponding particle image. The radial brightness distribution of the centro-symmetric pattern was then calculated, as schematically shown in Fig. 8B (bottom). Because of the diffraction and interference of the LED illumination (white, NVSW119BT, Audio-Q), the image center was dark (bright) when the microscope focus was slightly above (below) the particle. The PID feedback for the *z* position of the objective lens was set up such that brightness in the center and at the fringe of the particle pattern remained equal. A software-based PID loop was created on a PC equipped with a signal generator (NI PXI 6221, National Instruments) that supplied a real-time voltage signal that was fed to the *z* axis piezo scanner that held the objective (PIFOC 72Z1, Physik Instrumente GmbH & Co. KG). The particle pattern was therefore maintained, as shown in the leftmost images in the three panels in Fig. 8B, when the *z* axis feedback was active.

Calibration of laser interferometry displacement detection and trap stiffness in cells

The probe displacement $u_{QPD}(t)$ and the applied optical trapping force $F(t)$ were obtained by calibrating the output voltage $V(t)$ of QPDs for both the probe and the drive lasers. For dilute samples with a refractive index nearly identical to that of the solvent (for example, actin in watery

buffer or PAAm gels), the trap stiffness (the effective spring constant) $k \equiv F(t)/u_{QPD}$ and the calibration factor for the displacement response of the QPD $C \equiv u_{QPD}(t)/V(t)$ were obtained by analyzing the Brownian motion of the probe beads in pure solvent (*14*, *16*).

This conventional calibration method is, however, not valid in living cells. The refractive index in cells depends on particulars, such as the cell type, osmotic pressure of culture media, location in the cell, and the determination method. Measured values for most animal cells are $n_{cell} \sim 1.38 \pm 0.02$, larger than that of water ($n_{water} = 1.33$) (*61*–*66*). Here, the trap stiffness k_{cell} and the calibration factor C_{cell} in the cells were estimated using the following three-step procedure: (i) With the laser focused on the bead, the piezo stage was oscillated with feedback at ~0.5 Hz in the *x* or *y* direction to oscillate the probe bead sinusoidally through the focus of the low-power superimposed laser focus. By recording the video images and the QPD output from the low-power laser simultaneously, we obtained C_{cell} by directly comparing the amplitudes of $u(t)$ and $V(t)$. This procedure was carried out for every particle, which we observed in cells, and eliminates the errors due to, for example, inhomogeneities in cells and distributions of probe properties. (ii) The Brownian motion of probe particles was measured in an aqueous mixture containing 40 weight % (wt %) glycerol, which has a refractive index similar to that of cells (*67*). Probe particles were trapped at a height above the glass-medium interface that was close to that of the experiments in cells, to reduce the effect of the spherical aberration and/or the effect of the optical interference near the coverslip surface (*68*–*70*). Using the known viscosity of the mixture of ~2.2×10^{-3} Pa·s at 37°C, the power spectrum of the Brownian motion provided the values for both k_g and C_g in the solution. (iii) Because both k and $1/C$ (diffraction efficiency) are proportional to the effective polarizability of the probe, an approximately inverse relation between k and C holds (see fig. S7) (*29*, *71*). When the laser power and its profile are equal, k_{cell} can therefore be obtained using $k_{cell} = k_g C_g / C_{cell}$ (see note S4). Although the trap force calibration does not eliminate the effect of probe-size distribution, polydispersity (<5%) is small and only marginally affects our experiment (*16*).

Feedback AMR from measured voltage signals

In the actual AMR measurements (Fig. 2), the measured electric signals were $V(t)$ and $\varepsilon(t)$, neither of which is directly proportional to the total displacement $u(t)$. The lock-in amplifier converts these signals and provides outputs $\langle \hat{V}(\omega) \rangle$ and $\langle \hat{\varepsilon}(\omega) \rangle$. Theoretically, the intrinsic response function $\alpha(\omega)$ and the shear elastic modulus $G(\omega)$ can be derived from either of these outputs, if the calibration factors B and C, as well as the correction parameters k_t and τ, are known. Therefore, there are two procedures to perform AMR in the feedback mode based on the measured signals. The first option is to use the output of the QPD, $\langle \hat{V}(\omega) \rangle = \langle \hat{u}_{QPD}(\omega) \rangle / C$. Here, we define the apparent response function $A_{QPD}(\omega)$ as the ratio of $\langle \hat{u}_{QPD}(\omega) \rangle$ to the applied force $\hat{F}(\omega)$. By substituting Eq. 4 into Eq. 2 to eliminate $\hat{u}_{stage}$, we obtain

$$A_{QPD}(\omega) \equiv \frac{\langle \hat{u}_{QPD}(\omega) \rangle}{\hat{F}(\omega)} = \frac{1}{1 + \beta\alpha(\omega)} \cdot \frac{-i\omega\tau\alpha(\omega)}{1 - i\omega\tau} \quad (10)$$

Thus, $\alpha(\omega)$ is obtained from the measured $\langle \hat{V}(\omega) \rangle$ as

$$\alpha(\omega) = \frac{k_t}{\beta} \cdot \frac{A_{QPD}(\omega)}{1 - k_t A_{QPD}(\omega)} = -\frac{(1 - i\omega\tau) C \langle \hat{V}(\omega) \rangle}{i\omega\tau \left(\hat{F}(\omega) - k_t C \langle \hat{V}(\omega) \rangle \right)} \quad (11)$$

where the relation $A_{QPD}(\omega) = C \langle \hat{V}(\omega) \rangle / \hat{F}(\omega)$ has been applied.

The alternative procedure is to use the output of the PID controller $\langle \hat{\varepsilon}(\omega) \rangle = \langle u_{stage}(\omega) \rangle / B$ instead of that of the QPD. Substituting Eq. 4 into Eq. 2 to eliminate $\hat{u}_{QPD}$, we obtain the following expression

$$A_{stage}(\omega) \equiv \frac{\langle \hat{u}_{stage}(\omega) \rangle}{\hat{F}(\omega)} = \frac{1}{1 + \beta\alpha(\omega)} \cdot \frac{\alpha(\omega)}{1 - i\omega\tau} \quad (12)$$

where $A_{stage}(\omega)$ is defined as the response function for the position of the feedback-controlled piezo stage. Thus, $a(\omega)$ can be estimated from $\langle \hat{\varepsilon}(\omega) \rangle$ as

$$\alpha(\omega) = \frac{k_t}{\beta} \cdot \frac{-i\omega\tau A_{stage}}{1 + i\omega\tau k_t A_{stage}} = \frac{(1 - i\omega\tau) B \langle \hat{\varepsilon}(\omega) \rangle}{\hat{F}(\omega) + i\omega\tau k_t B \langle \hat{\varepsilon}(\omega) \rangle} \quad (13)$$

As can be seen from Eqs. 5, 10, and 12, $A_{FB} = A_{QPD} + A_{stage}$. This relation is the direct consequence of $u = u_{QPD} + u_{stage}$. In both cases, the shear viscoelastic modulus can be obtained from $\alpha(\omega)$ via Eq. 6.

Feedback PMR far from equilibrium

Suppose that a nonthermal fluctuating force $f(t) \neq 0$ is acting on the probe particle and that $f(t)$ is not correlated with the thermal fluctuating force $\zeta(t)$. The Fourier transform of eq. S1 in note S1 after setting $L = 0$ yields $\langle |\tilde{u}(\omega)|^2 \rangle^{trap}$ for the case in which no feedback is applied (that is, the conventional PMR). The PSD can then be obtained by summing the thermal and nonthermal fluctuations: $\langle |\tilde{u}(\omega)|^2 \rangle^{trap} = |A(\omega)|^2 \left\{ \langle |\tilde{\zeta}(\omega)|^2 \rangle + \langle |\tilde{f}(\omega)|^2 \rangle \right\}$. The trap-corrected fluctuations $\langle |\tilde{u}(\omega)|^2 \rangle^{no\ trap}$, on the other hand, can be expressed as

$$\langle |\tilde{u}(\omega)|^2 \rangle^{no\ trap} = |\alpha(\omega)|^2 \left\{ \langle |\tilde{\zeta}(\omega)|^2 \rangle + \langle |\tilde{f}(\omega)|^2 \rangle \right\} \quad (14)$$

If $\alpha(\omega)$ is independently measured with AMR, then the effects of the optical trap in $\langle |\tilde{u}(\omega)|^2 \rangle^{trap}$ can be corrected using $\langle |\tilde{u}(\omega)|^2 \rangle^{no\ trap} = |1 + k_t\alpha(\omega)|^2 \langle |\tilde{u}(\omega)|^2 \rangle^{trap} = \langle |\tilde{u}(\omega)|^2 \rangle^{trap} / |1 - k_t A(\omega)|^2$ (*18*).

For the feedback PMR experiments, the PSD of $u = u_{QPD} + u_{stage}$ can be written as $\langle |\tilde{u}(\omega)|^2 \rangle^{FB} = |A_{FB}(\omega)|^2 \left\{ \langle |\tilde{\zeta}(\omega)|^2 \rangle + \langle |\tilde{f}(\omega)|^2 \rangle \right\}$, using the response function $A_{FB}(\omega)$ defined in Eq. 5 in Results. The fluctuations in the absence of optical trapping and feedback can then be estimated by independently measuring $\alpha(\omega)$ via AMR, as well as k_t and τ, as shown in the experimental section and note S1. The resulting equation $\langle |\tilde{u}(\omega)|^2 \rangle^{no\ trap} = |1 + \beta\alpha(\omega)|^2 \langle |\tilde{u}(\omega)|^2 \rangle^{FB}$ is apparently equal to Eq. 9 in Results. However, this time, the FDT is not satisfied because of the additional fluctuation generated by the nonthermal force $\langle |\tilde{u}(\omega)|^2 \rangle^{nonthermal} = |\alpha(\omega)|^2 \langle |\tilde{f}(\omega)|^2 \rangle$. Assuming that the FDT is valid for the thermal part of the fluctuations in Eq. 14, that is, $|\alpha(\omega)|^2 \langle |\tilde{\zeta}(\omega)|^2 \rangle = 2k_B T\alpha''/\omega$, nonthermal fluctuations $\langle |\tilde{u}(\omega)|^2 \rangle^{nonthermal}$ occurring in far-from-equilibrium systems, such as living cells, can then be related to the violation of the FDT using

$$\langle |\tilde{u}(\omega)|^2 \rangle^{nonthermal} = \langle |\tilde{u}(\omega)|^2 \rangle^{no\ trap} - \frac{2k_B T\alpha''}{\omega} = |\alpha(\omega)|^2 \langle |\tilde{f}(\omega)|^2 \rangle \quad (15)$$

Gel preparation

Gels consisting of 1.75 wt % PAAm were prepared with 30 wt % acrylamide/bis-acrylamide mixed solution (37.5:1, Wako Chemicals Inc.),

polystyrene beads (Polysciences Inc., $2a$ = 2 μm diameter), and 0.033% ammonium persulfate. The solution was thoroughly degassed in a vacuum, and polymerization was initiated by adding 0.05% tetramethylethylenediamine. The solution was loaded into a glass chamber and polymerized at room temperature for several hours while the chamber was gently rotated. This thermal equilibrium sample was measured by feedback AMR with the following calibration values: $k_p = 9.4 \times 10^{-7}$ N/m, $k_d = 5.8 \times 10^{-6}$ N/m, and $\tau = 3.8 \times 10^{-2}$ s ($I = 2\ s^{-1}$, $C = 4.1 \times 10^{-7}$ m/V, $B = 5.4 \times 10^{-6}$ m/V).

G-actin was prepared from rabbit skeletal muscle according to standard protocols (*72*) and was stored at −80°C in G-buffer [2 mM tris-Cl, 0.2 mM $CaCl_2$, 0.5 mM DTT, and 0.2 mM ATP (pH 7.5)]. G-actin was diluted into F-buffer [1 mM Na_2ATP, 2 mM Hepes, 1 mM EGTA, 2 mM $MgCl_2$, and 50 mM KCl (pH 7.5)] to initiate actin polymerization. An F-actin solution (1 mg/ml) including polystyrene beads (Polysciences Inc., $2a$ = 1 μm diameter) was directly infused into sample chambers. Polymerization occurred at room temperature for about 30 min. The thermal equilibrium sample was then measured by feedback PMR with the following calibration values: $k_t = k_p = 4.8 \times 10^{-6}$ N/m and $\tau = 0.024$ s.

Cell preparation

Mouse fibroblasts (NIH-3T3) were cultivated on fibronectin-coated glass-bottom petri dishes in Dulbecco's modified Eagle's medium with glucose (1 mg/ml), penicillin (100 U/ml), streptomycin (0.1 mg/ml), and 10% fetal bovine serum at 37°C. When the population of cells in a flask was semiconfluent, the medium was replaced by a CO_2-independent culture medium (Gibco) without serum, containing melamine resin particles (diameter, 680 nm; refractive index, 1.68; polydispersity, <5%; microParticles GmbH) as probe beads. The dishes were then incubated for several hours until the beads were phagocytosed. Excess beads were removed by washing the dishes with phosphate-buffered saline. Finally, a CO_2-independent culture medium without probe beads was added to perform the measurements. The mechanical properties were measured by feedback MR with the following calibration values: $k_p = 1.2 \times 10^{-5}$ N/m and $k_d = 5.1 \times 10^{-5}$ N/m.

HeLa cells were seeded on fibronectin-coated glass-bottom petri dishes in the same culture medium as above, except that this medium included amphotericin B (250 mg/ml). When the population of cells in a flask was confluent, the medium was replaced by a CO_2-independent culture medium (Wako). The probe particles [melamine particles coated with PEG (*39*); diameter, $2a$ = 1 μm; refractive index, 1.68; polydispersity, <5%; microParticles GmbH] were introduced into the HeLa cells using a gene gun (PDS-1000/He, Bio-Rad). PEG coating has been widely used to study biomaterials with MR to generally passivate probe surfaces. In aqueous environments, hydrophilic PEG acts as a polymer brush and prevents sticking to other objects or to other molecules. Because this barrier is merely nanometers thick it does not prevent the micrometer-sized beads from hydrodynamically coupling to their surroundings (*16*, *18*, *73*). The dishes were then placed in an incubator for at least several hours until the cell membranes recovered. Excess beads were removed by washing the dishes with phosphate-buffered saline. Finally, a CO_2-independent culture medium without serum was added to perform the measurements. Macromolecular concentrations in cells were varied by osmotic compression (*55*). Intracellular macromolecular concentration was systematically increased by adding sucrose to the culture media, thus increasing the osmotic pressure. The volume fraction of intracellular macromolecules was estimated from the ionic strength of the medium according to Ponder's law (*74*). The mechanical properties were measured by feedback MR with the following trap stiffnesses: $k_p \sim 1 \times 10^{-6}$ N/m and $k_d \sim 1 \times 10^{-5}$ N/m. The temperature increase due to the drive laser (<100 mW) will be at most 1°–2°C at the beam focus (*75*). To characterize cells that are more sensitive than the ones used in this study or to be able to perform time-lapse experiments over extended periods of time, the laser power can be further reduced to ~10 mW (causing less than a ~0.2°C temperature increase). In addition, it has been shown that laser wavelengths of 830 or 970 nm cause the least nonthermal damage in cells (*76*).

For comparison, cytoplasmic extracts of HeLa cells (CC-01-40-25, Cilbiotech) were used. As purchased, they contain most of the intracellular contents except the membrane fraction and nuclear components. When we used these extracts, cytoskeleton polymerization was inhibited by 0.1 mM cytochalasin B, and molecules smaller than 3 kDa were removed by filtration to inhibit metabolic activity.

SUPPLEMENTARY MATERIALS

Supplementary material for this article is available at http://advances.sciencemag.org/cgi/content/full/3/9/e1700318/DC1

note S1. Conventional AMR without feedback control.
note S2. Response time measurement of the feedback system.
note S3. Conventional PMR in thermal equilibrium.
note S4. Inverse proportionality between *k* and *C*.
fig. S1. Experimental test of feedback performance.
fig. S2. Imaginary part of the response functions of a probe in a PAAm gel.
fig. S3. Apparent violation of the FDT under feedback.
fig. S4. Complex shear modulus in HeLa cells measured with feedback AMR.
fig. S5. PSD obtained under feedback PMR in actin solution.
fig. S6. Fluctuation and mechanical property in actin/myosin active gel.
fig. S7. Inversely proportional relationship between trap stiffness and displacement response used for calibration in cells.

REFERENCES AND NOTES

1. D. Mizuno, R. Bacabac, C. Tardin, D. Head, C. F. Schmidt, High-resolution probing of cellular force transmission. *Phys. Rev. Lett.* **102**, 168102 (2009).
2. D. Mizuno, C. Tardin, C. F. Schmidt, F. C. MacKintosh, Nonequilibrium mechanics of active cytoskeletal networks. *Science* **315**, 370–373 (2007).
3. B. Fabry, G. N. Maksym, J. P. Butler, M. Glogauer, D. Navajas, J. J. Fredberg, Scaling the microrheology of living cells. *Phys. Rev. Lett.* **87**, 148102 (2001).
4. P. Bursac, G. Lenormand, B. Fabry, M. Oliver, D. A. Weitz, V. Viasnoff, J. P. Butler, J. J. Fredberg, Cytoskeletal remodelling and slow dynamics in the living cell. *Nat. Mater.* **4**, 557–561 (2005).
5. M. L. Gardel, J. H. Shin, F. C. MacKintosh, L. Mahadevan, P. Matsudaira, D. A. Weitz, Elastic behavior of cross-linked and bundled actin networks. *Science* **304**, 1301–1305 (2004).
6. G. H. Koenderink, Z. Dogic, F. Nakamura, P. M. Bendix, F. C. MacKintosh, J. H. Hartwig, T. P. Stossel, D. A. Weitz, An active biopolymer network controlled by molecular motors. *Proc. Natl. Acad. Sci. U.S.A.* **106**, 15192–15197 (2009).
7. D. A. Head, E. Ikebe, A. Nakamasu, P. Zhang, L. G. Villaruz, S. Kinoshita, S. Ando, D. Mizuno, High-frequency affine mechanics and nonaffine relaxation in a model cytoskeleton. *Phys. Rev. E* **89**, 042711 (2014).
8. D. A. Head, D. Mizuno, Local mechanical response in semiflexible polymer networks subjected to an axisymmetric prestress. *Phys. Rev. E* **88**, 022717 (2013).
9. T. G. Mason, J. Bibette, D. A. Weitz, Yielding and flow of monodisperse emulsions. *J. Colloid Interface Sci.* **179**, 439–448 (1996).
10. P. Sollich, F. Lequeux, P. Hebraud, M. E. Cates, Rheology of soft glassy materials. *Phys. Rev. Lett.* **78**, 2020–2023 (1997).
11. X. Trepat, L. Deng, S. S. An, D. Navajas, D. J. Tschumperlin, W. T. Gerthoffer, J. P. Butler, J. J. Fredberg, Universal physical responses to stretch in the living cell. *Nature* **447**, 592–595 (2007).
12. R. Krishnan, C. Y. Park, Y.-C. Lin, J. Mead, R. T. Jaspers, X. Trepat, G. Lenormand, D. Tambe, A. V. Smolensky, A. H. Knoll, J. P. Butler, J. J. Fredberg, Reinforcement versus fluidization in cytoskeletal mechanoresponsiveness. *PLOS ONE* **4**, e5486 (2009).

13. T. G. Mason, D. A. Weitz, Optical measurements of frequency-dependent linear viscoelastic moduli of complex fluids. *Phys. Rev. Lett.* **74**, 1250–1253 (1995).
14. F. Gittes, C. F. Schmidt, Signals and noise in micromechanical measurements. *Methods Cell Biol.* **55**, 129–156 (1998).
15. T. G. Mason, K. Ganesan, J. H. van Zanten, D. Wirtz, S. C. Kuo, Particle tracking microrheology of complex fluids. *Phys. Rev. Lett.* **79**, 3282–3285 (1997).
16. B. Schnurr, F. Gittes, F. C. MacKintosh, C. F. Schmidt, Determining microscopic viscoelasticity in flexible and semiflexible polymer networks from thermal fluctuations. *Macromolecules* **30**, 7781–7792 (1997).
17. J. Xu, A. Palmer, D. Wirtz, Rheology and microrheology of semiflexible polymer solutions: Actin filament networks. *Macromolecules* **31**, 6486–6492 (1998).
18. D. Mizuno, D. A. Head, F. C. MacKintosh, C. F. Schmidt, Active and passive microrheology in equilibrium and nonequilibrium systems. *Macromolecules* **41**, 7194–7202 (2008).
19. L. A. Hough, H. D. Ou-Yang, Correlated motions of two hydrodynamically coupled particles confined in separate quadratic potential wells. *Phys. Rev. E* **65**, 021906 (2002).
20. D. Mizuno, Y. Kimura, R. Hayakawa, Electrophoretic microrheology in a dilute lamellar phase of a nonionic surfactant. *Phys. Rev. Lett.* **87**, 088104 (2001).
21. L. D. Landau, E. M. Lifshiëtis, L. P. Pitaevskiæi, *Statistical Physics*, (Pergamon Press, ed. 3, 1980).
22. A. W. C. Lau, B. D. Hoffman, A. Davies, J. C. Crocker, T. C. Lubensky, Microrheology, stress fluctuations, and active behavior of living cells. *Phys. Rev. Lett.* **91**, 198101 (2003).
23. T. Harada, S.-i. Sasa, Equality connecting energy dissipation with a violation of the fluctuation-response relation. *Phys. Rev. Lett.* **95**, 130602 (2005).
24. D. A. Head, D. Mizuno, Nonlocal fluctuation correlations in active gels. *Phys. Rev. E* **81**, 041910 (2010).
25. B. D. Hoffman, G. Massiera, K. M. Van Citters, J. C. Crocker, The consensus mechanics of cultured mammalian cells. *Proc. Natl. Acad. Sci. U.S.A.* **103**, 10259–10264 (2006).
26. Y. Tseng, T. P. Kole, D. Wirtz, Micromechanical mapping of live cells by multiple-particle-tracking microrheology. *Biophys. J.* **83**, 3162–3176 (2002).
27. R. E. Thompson, D. R. Larson, W. W. Webb, Precise nanometer localization analysis for individual fluorescent probes. *Biophys. J.* **82**, 2775–2783 (2002).
28. M. Guo, A. J. Ehrlicher, M. H. Jensen, M. Renz, J. R. Moore, R. D. Goldman, J. Lippincott-Schwartz, F. C. Mackintosh, D. A. Weitz, Probing the stochastic, motor-driven properties of the cytoplasm using force spectrum microscopy. *Cell* **158**, 822–832 (2014).
29. F. Gittes, C. F. Schmidt, Interference model for back-focal-plane displacement detection in optical tweezers. *Opt. Lett.* **23**, 7–9 (1998).
30. C. Storm, J. J. Pastore, F. C. MacKintosh, T. C. Lubensky, P. A. Janmey, Nonlinear elasticity in biological gels. *Nature* **435**, 191–194 (2005).
31. M. Atakhorrami, J. I. Sulkowska, K. M. Addas, G. H. Koenderink, J. X. Tang, A. J. Levine, F. C. Mackintosh, C. F. Schmidt, Correlated fluctuations of microparticles in viscoelastic solutions: Quantitative measurement of material properties by microrheology in the presence of optical traps. *Phys. Rev. E* **73**, 061501 (2006).
32. M. Guo, A. J. Ehrlicher, S. Mahammad, H. Fabich, M. H. Jensen, J. R. Moore, J. J. Fredberg, R. D. Goldman, D. A. Weitz, The role of vimentin intermediate filaments in cortical and cytoplasmic mechanics. *Biophys. J.* **105**, 1562–1568 (2013).
33. M. Röding, M. Guo, D. A. Weitz, M. Rudemo, A. Särkkä, Identifying directional persistence in intracellular particle motion using Hidden Markov Models. *Math. Biosci.* **248**, 140–145 (2014).
34. N. Fakhri, A. D. Wessel, C. Willms, M. Pasquali, D. R. Klopfenstein, F. C. MacKintosh, C. F. Schmidt, High-resolution mapping of intracellular fluctuations using carbon nanotubes. *Science* **344**, 1031–1035 (2014).
35. R. N. Zia, B. J. Landrum, W. B. Russel, A micro-mechanical study of coarsening and rheology of colloidal gels: Cage building, cage hopping, and Smoluchowski's ratchet. *J. Rheol.* **58**, 1121–1157 (2014).
36. A. J. Liu, S. Ramaswamy, T. G. Mason, H. Gang, D. A. Weitz, Anomalous viscous loss in emulsions. *Phys. Rev. Lett.* **76**, 3017–3020 (1996).
37. F. Gittes, B. Schnurr, P. D. Olmsted, F. C. MacKintosh, C. F. Schmidt, Microscopic viscoelasticity: Shear moduli of soft materials determined from thermal fluctuations. *Phys. Rev. Lett.* **79**, 3286–3289 (1997).
38. M. Doi, S. F. Edwards, *The Theory of Polymer Dynamics* (Clarendon Press, 1986).
39. J. He, J. X. Tang, Surface adsorption and hopping cause probe-size-dependent microrheology of actin networks. *Phys. Rev. E* **83**, 041902 (2011).
40. P. Panorchan, J. S. H. Lee, T. P. Kole, Y. Tseng, D. Wirtz, Microrheology and ROCK signaling of human endothelial cells embedded in a 3D matrix. *Biophys. J.* **91**, 3499–3507 (2006).
41. A. K. Gupta, S. Wells, Surface modified superparamagnetic nanoparticles for drug delivery: Preparation, characterization, and cytotoxicity studies. *IEEE Trans. Nanobiosci.* **3**, 66–73 (2004).
42. F. Schlosser, F. Rehfeldt, C. F. Schmidt, Force fluctuations in three-dimensional suspended fibroblasts. *Philos. Trans. R. Soc. London Ser. B* **370**, 20140028 (2015).
43. H. Turlier, D. A. Fedosov, B. Audoly, T. Auth, N. S. Gov, C. Sykes, J.-F. Joanny, G. Gompper, T. Betz, Equilibrium physics breakdown reveals the active nature of red blood cell flickering. *Nat. Phys.* **12**, 513–519 (2016).
44. T. Toyota, D. A. Head, C. F. Schmidt, D. Mizuno, Non-Gaussian athermal fluctuations in active gels. *Soft Matter* **7**, 3234–3239 (2011).
45. F. C. MacKintosh, A. J. Levine, Nonequilibrium mechanics and dynamics of motor-activated gels. *Phys. Rev. Lett.* **100**, 018104 (2008).
46. F. Gittes, F. C. MacKintosh, Dynamic shear modulus of a semiflexible polymer network. *Phys. Rev. E* **58**, R1241–R1244 (1998).
47. G. H. Koenderink, M. Atakhorrami, F. C. MacKintosh, C. F. Schmidt, High-frequency stress relaxation in semiflexible polymer solutions and networks. *Phys. Rev. Lett.* **96**, 138307 (2006).
48. B. Alberts, A. Johnson, J. Lewis, D. Morgan, M. Raff, K. Roberts, P. Walter, *Molecular Biology of the Cell* (Garland Publishing Inc., ed. 6, 2015).
49. B. Fabry, G. N. Maksym, J. P. Butler, M. Glogauer, D. Navajas, N. A. Taback, E. J. Millet, J. J. Fredberg, Time scale and other invariants of integrative mechanical behavior in living cells. *Phys. Rev. E* **68**, 041914 (2003).
50. K. Kroy, J. Glaser, The glassy wormlike chain. *New J. Phys.* **9**, 416 (2007).
51. R. W. Mays, K. A. Beck, W. J. Nelson, Organization and function of the cytoskeleton in polarized epithelial cells: A component of the protein sorting machinery. *Curr. Opin. Cell Biol.* **6**, 16–24 (1994).
52. R. Bacallao, C. Antony, C. Dotti, E. Karsenti, E. H. Stelzer, K. Simons, The subcellular organization of Madin-Darby canine kidney-cells during the formation of a polarized epithelium. *J. Cell Biol.* **109**, 2817–2832 (1989).
53. G. L. Hunter, E. R. Weeks, The physics of the colloidal glass transition. *Rep. Prog. Phys.* **75**, 066501 (2012).
54. B. R. Parry, I. V. Surovtsev, M. T. Cabeen, C. S. O'Hem, E. R. Dufresne, C. Jacobs-Wagner, The bacterial cytoplasm has glass-like properties and is fluidized by metabolic activity. *Cell* **156**, 183–194 (2014).
55. E. H. Zhou, X. Trepat, C. Y. Park, G. Lenormand, M. N. Oliver, S. M. Mijailovich, C. Hardin, D. A. Weitz, J. P. Butler, J. J. Fredberg, Universal behavior of the osmotically compressed cell and its analogy to the colloidal glass transition. *Proc. Natl. Acad. Sci. U.S.A.* **106**, 10632–10637 (2009).
56. G. T. Charras, T. J. Mitchison, L. Mahadevan, Animal cell hydraulics. *J. Cell Sci.* **122**, 3233–3241 (2009).
57. J. Mattsson, H. M. Wyss, A. Fernandez-Nieves, K. Miyazaki, Z. Hu, D. R. Reichman, D. A. Weitz, Soft colloids make strong glasses. *Nature* **462**, 83–86 (2009).
58. Y. Nishigami, M. Ichikawa, T. Kazama, R. Kobayashi, T. Shimmen, K. Yoshikawa, S. Sonobe, Reconstruction of active regular motion in amoeba extract: Dynamic cooperation between sol and gel states. *PLOS ONE* **8**, e70317 (2013).
59. T. Nakagaki, R. D. Guy, Intelligent behaviors of amoeboid movement based on complex dynamics of soft matter. *Soft Matter* **4**, 57–67 (2008).
60. A. J. Liu, S. R. Nagel, Nonlinear dynamics: Jamming is not just cool any more. *Nature* **396**, 21–22 (1998).
61. K. G. Phillips, S. L. Jacques, O. J. T. McCarty, Measurement of single cell refractive index, dry mass, volume, and density using a transillumination microscope. *Phys. Rev. Lett.* **109**, 118105 (2012).
62. N. Lue, G. Popescu, T. Ikeda, R. R. Dasari, K. Badizadegan, M. S. Feld, Live cell refractometry using microfluidic devices. *Opt. Lett.* **31**, 2759–2761 (2006).
63. M. Sernetz, A. Thaer, Immersion refractometry on living cells with the method of refractive index gradient. *Z. Anal. Chem.* **252**, 90–93 (1970).
64. R. Barer, S. Joseph, Refractometry of living cells. 1. Basic principles. *Q. J. Microsc. Sci.* **95**, 399–423 (1954).
65. B. Rappaz, P. Marquet, E. Cuche, Y. Emery, C. Depeursinge, P. J. Magistretti, Measurement of the integral refractive index and dynamic cell morphometry of living cells with digital holographic microscopy. *Opt. Express* **13**, 9361–9373 (2005).
66. C. L. Curl, C. J. Bellair, T. Harris, B. E. Allman, P. J. Harris, A. G. Stewart, A. Roberts, K. A. Nugent, L. M. D. Delbridge, Refractive index measurement in viable cells using quantitative phase-amplitude microscopy and confocal microscopy. *Cytometry A* **65A**, 88–92 (2005).
67. Glycerine Producers Association, *Physical Properties of Glycerine and Its Solutions* (Glycerine Producers' Association, 1963).
68. K. C. Vermeulen, G. J. L. Wuite, G. J. M. Stienen, C. F. Schmidt, Optical trap stiffness in the presence and absence of spherical aberrations. *Appl. Opt.* **45**, 1812–1819 (2006).
69. K. C. Vermeulen, J. van Mameren, G. J. M. Stienen, E. J. G. Peterman, G. J. L. Wuite, C. F. Schmidt, Calibrating bead displacements in optical tweezers using acousto-optic deflectors. *Rev. Sci. Instrum.* **77**, 013704 (2006).
70. K. C. Neuman, S. M. Block, Optical trapping. *Rev. Sci. Instrum.* **75**, 2787–2809 (2004).
71. T. Tlusty, A. Meller, R. Bar-Ziv, Optical gradient forces of strongly localized fields. *Phys. Rev. Lett.* **81**, 1738–1741 (1998).

72. L. W. Cunningham, D. W. Frederiksen, R. B. Vallee, *Structural and Contractile Proteins* (Academic Press, 1982).
73. A. J. Levine, T. C. Lubensky, Two-point microrheology and the electrostatic analogy. *Phys. Rev. E* **65**, 011501 (2001).
74. H. P. Ting-Beall, D. Needham, R. M. Hochmuth, Volume and osmotic properties of human neutrophils. *Blood* **81**, 2774–2780 (1993).
75. E. J. G. Peterman, F. Gittes, C. F. Schmidt, Laser-induced heating in optical traps. *Biophys. J.* **84**, 1308–1316 (2003).
76. K. C. Neuman, E. H. Chadd, G. F. Liou, K. Bergman, S. M. Block, Characterization of photodamage to *Escherichia coli* in optical traps. *Biophys. J.* **77**, 2856–2863 (1999).

Acknowledgments

Funding: This work was supported by the Japan Society for the Promotion of Science KAKENHI (grant numbers JP15H01494, JP25127712, JP25103011, JP15H03710, and JP23684036 to D.M.; grant numbers JP25870173 and JP15K05248 to T.A.; and grant number JP15J04464 to K.N.). K.N. was also supported by the Sasakawa Scientific Research Grant from the Japan Science Society (grant number 26–219). C.F.S. was supported by the Deutsche Forschungsgemeinschaft Collaborative Research Center SFB 937 (Project A2) and the European Research Council Advanced Grant FP7 ERC-2013-AdG, Project 324 340528. **Author contributions:** K.N. and M.B. conducted experiments and analysis. H.A. provided an analysis script. D.M. designed the research. D.M., K.N., M.B., T.A., and C.F.S. discussed the results and wrote the manuscript. **Competing interests:** The authors declare that they have no competing interests. **Data and materials availability:** All data needed to evaluate the conclusions in the paper are present in the paper and/or the Supplementary Materials. Additional data related to this paper may be requested from the authors.

Submitted 31 January 2017
Accepted 7 September 2017
Published 29 September 2017
10.1126/sciadv.1700318

Citation: K. Nishizawa, M. Bremerich, H. Ayade, C. F. Schmidt, T. Ariga, D. Mizuno, Feedback-tracking microrheology in living cells. *Sci. Adv.* **3**, e1700318 (2017).

Feedback-tracking microrheology in living cells

Kenji Nishizawa, Marcel Bremerich, Heev Ayade, Christoph F. Schmidt, Takayuki Ariga and Daisuke Mizuno

Sci Adv **3** (9), e1700318.
DOI: 10.1126/sciadv.1700318